Nano Research
2020, 13(1): 151–159

ISSN 1998-0124 CN 11-5974/O4
https://doi.org/10.1007/s12274-019-2588-0

Research Article

Mitigation of voltage decay in Li-rich layered oxides as cathode materials for lithium-ion batteries

Wenhui Hu[1], Youxiang Zhang[1,2] (✉), Ling Zan[1], and Hengjiang Cong[1] (✉)

[1] College of Chemistry and Molecular Sciences, Wuhan University, Wuhan 430072, China
[2] Shenzhen Research Institute of Wuhan University, Shenzhen 518000, China

Received: 6 October 2019 / **Revised:** 25 November 2019 / **Accepted:** 28 November 2019

ABSTRACT

Lithium-rich layered oxides (LLOs) have been extensively studied as cathode materials for lithium-ion batteries (LIBs) by researchers all over the world in the past decades due to their high specific capacities and high charge-discharge voltages. However, as cathode materials LLOs have disadvantages of significant voltage and capacity decays during the charge-discharge cycling. It was shown in the past that fine-tuning of structures and compositions was critical to the performances of this kind of materials. In this report, LLOs with target composition of $Li_{1.17}Mn_{0.50}Ni_{0.24}Co_{0.09}O_2$ were prepared by carbonate co-precipitation method with different pH values. X-ray powder diffraction (XRD), scanning electron microscopy (SEM), transmission electron microscope (TEM), and electrochemical impedance spectroscopies (EIS) were used to investigate the structures and morphologies of the materials and to understand the improvements of their electrochemical performances. With the pH values increased from 7.5 to 8.5, the Li/Ni ratios in the compositions decreased from 5.17 to 4.64, and the initial Coulombic efficiency, cycling stability and average discharge voltages were gained impressively. Especially, the material synthesized at pH = 8.5 delivered a reversible discharge capacity of 263 mAh·g^{-1} during the first cycle, with 79.0% initial Coulombic efficiency, at the rate of 0.1 C and a superior capacity retention of 94% after 100 cycles at the rate of 1 C. Furthermore, this material exhibited an initial average discharge voltage of 3.65 V, with a voltage decay of only 0.09 V after 50 charge-discharge cycles. The improved electrochemical performances by varying the pH values in the synthesis process can be explained by the mitigation of layered-to-spinel phase transformation and the reduction of solid-electrolyte interface (SEI) resistance. We hope this work can shed some light on the alleviation of voltage and capacity decay issues of the LLOs cathode materials.

KEYWORDS

lithium ion batteries, cathode, lithium-rich layered oxides, voltage decay, $Li_{1.17}Mn_{0.50}Ni_{0.24}Co_{0.09}O_2$

1 Introduction

Rechargeable lithium-ion batteries (LIBs) are an integral part of people's modern life due to their large scale applications in portable electronic devices (such as cellphones) and electrical vehicles. High capacities, high energy densities and power densities, low cost and long lifespans are the key factors in the practical applications of LIBs [1–3]. Among the cathode materials that are used practically for LIBs at present, layered oxides with a general formula $LiMO_2$ (M = $Ni_xMn_yCo_{1-x-y}$; $0 \le x, y \le 1$) exhibit the highest capacity (~ 200 mAh·g^{-1}). By replacing part of M in the metal layers with the Li ions, researchers have developed a family of Li-rich layered oxides (LLOs), which exhibit higher capacities (> 250 mAh·g^{-1}) [4, 5]. Concerning the chemical nature of this family of LLOs, there are still discrepancies. With some researchers believe that LLOs are solid solutions having a sole monoclinic symmetry [6], many researchers consider the LLOs as composite oxides comprising monoclinic Li_2MnO_3 and trigonal $LiMO_2$ and thus usually write the LLOs as $xLi_2MnO_3\cdot(1-x)LiMO_2$ [7, 8]. By complementary X-ray photoelectron spectroscopy (XPS) and electron paramagnetic resonance (EPR), the extra high capacity of the LLOs is shown to be nested in reversible anionic redox processes by forming peroxo-like dimers [9–12] and/or formation of localized electron holes on anionic oxygen atoms coordinated by transition metal and lithium ions [13, 14].

Although with high capacity and high operating potentials, the LLOs are seldom used in practical cells owing to poor electrode kinetics and large voltage decays on charge-discharge cycling. This voltage decay is generally ascribed to the gradual layered-to-spinel structure evolution and thus formation of spinel-like domains in the layered crystal structure when cycled continuously at high voltages above 4.5 V [15–23]. During this layered-to-spinel phase transition, the transition metal (TM) ions migrate from TM-layer octahedral site to Li-layer octahedral site through Li-layer tetrahedral site [19, 20]. Improper solid-electrolyte interface (SEI) film formation resulted from the side reactions between electrode and electrolyte at high operation voltages exacerbate the situation [24, 25]. Particles structure defects, such as atomic non-uniformity, lattice distortion, and dislocation, also facilitate the layered-to-spinel transition [26, 27].

Extensive research has been carried out to explore effective approaches for suppressing the continuously voltage decay of LLOs materials. Doping the LLOs materials with cationic ions, such as Na, K, Mg, Fe and Al, is a strategy that has been studied for alleviating the voltage fading during the charge-discharge

Address correspondence to Youxiang Zhang, yxzhang04@whu.edu.cn; Hengjiang Cong, conghj@whu.edu.cn

cycling [28–32]. The ions doped in the lithium layer (Na and K ions) can stabilize the structures due to the fact that the doped ions can weaken the formation of trivacancies in lithium layer and the migration of Mn to form spinel structure. At the same time the doped ions have larger ionic radius than the Li ions which can aggravate steric hindrance for the spinel growth [28, 29]. The average discharge voltage decay upon cycling can be suppressed also by substituting the Mn in the transition metal layers with Al and Mg [30, 31] or substituting the Co in the transition metals with Fe [32]. The structural analysis of the cycled electrodes indicates that these ions doping can help stabilizing the layered phase by suppressing the layered-to-spinel phase transformation upon cycling. Another strategy that has been widely used to enhance the stability of the structures and improve the electrochemical performances of the LLOs is coating the surfaces of the LLOs with metal fluorides, metal oxides or metal phosphates [33–38]. Fundamental research demonstrates that these coating layers on the electrode particles can reduce the oxidation of the electrolyte at high voltage and protect the particles from severe etching by the acidic species in the electrolyte. The surface coating layers thus suppress the accumulation of thick SEI layers on particle surfaces and reduce the formation of etched and corrosion pits on the electrode particles. These protective coatings mitigate the layered-to-spinel phase transformation in the bulk region of the material and alleviate the undesirable voltage fade during the charge-discharge cycling. Electrochemically active $LiFePO_4$ layer was once coated onto the surface of $Li_{1.2}Mn_{0.54}Ni_{0.13}Co_{0.13}O_2$ and this Li-rich layered oxide coated with 5 wt.% $LiFePO_4$ demonstrated a discharge capacity of 282.8 mAh·g^{-1} at 0.1 C with capacity retention of 98.1% after 120 charge-discharge cycles [38]. Smart designs of structures have also been adopted to effectively inhibit the capacity and voltage fading of the LLOs cathodes. For example, $Li[Li_{0.2}Ni_{0.2}Mn_{0.6}]O_2$ with atomic level uniformity of Ni distribution prepared by a hydrothermal-assisted method exhibited minimal Ni-rich surfaces, leading to only a ~ 0.15 V decrease in the average discharge voltage over 200 cycles [39].

In the present work, LLO cathode materials with target chemical formula of $Li_{1.17}Mn_{0.50}Ni_{0.24}Co_{0.09}O_2$ have been synthesized by co-precipitation method, and the effects of synthetic pH parameter on the regulation of average discharge voltages and the discharge voltage decays have been studied. X-ray powder diffraction (XRD), scanning electron microscopy (SEM), transmission electron microscope (TEM), and electrochemical impedance spectroscopies (EIS) have been used to investigate the structures and morphologies of the materials synthesized at different pH values and to understand the reasons of the electrochemical performance improvements. It has been shown that the initial Coulombic efficiency, cycle stability and average discharge voltage can all be impressively improved when the synthesis pH values are increased from 7.5 to 8.5.

2 Experimental

Carbonate precursors were prepared by co-precipitation method, and the LLO cathode material $Li_{1.17}Mn_{0.50}Ni_{0.24}Co_{0.09}O_2$ was prepared by two annealing steps. The details are as follows. $MnSO_4·H_2O$, $NiSO_4·6H_2O$ and $CoSO_4·7H_2O$ (Mn:Ni:Co = 0.594:0.294:0.112) were dissolved in distilled water with a total concentration of 2 M. The 2 M MSO_4 solution was pumped into a continuously stirred tank reactor (CSTR) under N_2 atmosphere. Simultaneously, 2 M Na_2CO_3 solution and 0.2 M $NH_3·H_2O$ were pumped separately into the reactor. Temperatures of the mixed solutions were kept at 55 °C and the pH values of the mixed solution were fixed at 8.5, 8.2, 7.8 and 7.5, respectively. After 20 h aging reaction, the co-precipitated carbonate precursors were filtered, washed, and dried at 100 °C. The prepared carbonate precursors were then mixed with Li_2CO_3 (5% excess), preheated at 500 °C for 5 h and calcined at 850 °C for 15 h. Lastly, the products were cooled to room temperature naturally. The materials synthesized at 4 different pH values were marked as LMNCO-8.5, LMNCO-8.2, LMNCO-7.8 and LMNCO-7.5, respectively.

The crystal structures of the materials were characterized by powder X-ray diffraction (XRD, Bruker D8 ADVANCE). The XRD spectra were collected in the 2θ range of 10°–80°. Morphologies and detailed structure characterizations of the materials were observed by field effect scanning electron microscope (FESEM, Zeiss SIGMA) and transmission electron microscope (TEM, JEM-2100, JEOL Ltd.). The Li, Mn, Ni and Co molar ratios in the materials were analyzed by inductively coupled plasma atomic emission spectrometry (ICP-AES, IRIS Intrepid II XSP, Thermo Fisher Scientific USA). In order to further elucidate the local structure of these Li-rich layered oxides, we also performed a detailed structural analysis on a randomly selected nanoparticle from the as-prepared composites by the technique of TEM. All bright-field TEM micrographs, high-resolution TEM (HRTEM) micrographs, scanning transmission electron microscopy high-angle annular dark-field (STEM-HAADF) micrographs, energy-dispersive X-ray spectroscopy (EDX) elemental maps and selected-area electron diffraction (SAED) images were obtained using a JEOL JEM-2100F microscope operated at 200 keV and equipped with JEOL JED-2300 EDX system.

The electrochemical properties were tested using CR2016 coin-type cell with lithium metal disks as the counter electrodes. The working electrodes were made by pressing mixtures of active materials, acetylene black and poly(vinyl difluoride) binder with a weight ratio 80:15:5 on Al foils which were used as the current collectors. The weight of active materials in the cathode electrode varied between 3.0 and 4.0 mg for each cell. The electrolytes of the cells were composed by $LiPF_6$ (1 mol·L^{-1}) in the solvent of ethylene carbonate and dimethyl carbonate (1:1 v/v). The separators in the cells were Celgard 2300 microporous films. The cells were assembled in glovebox filled with high purity Ar gas. The electrochemical tests were performed galvanostatically at different current densities with voltage window of 2.0–4.8 V and 2.0–4.6 V on Neware battery test system (Shenzhen, China) at room temperature. EIS were conducted using a CHI760C electrochemistry workstation. The AC amplitude was 5 mV, and the applied frequency range was from 100 kHz to 0.01 Hz.

3 Results and discussion

A schematic of the water jacketed CSTR system is illustrated in Fig. S1 in the Electronic Supplementary Material (ESM), which is used for the co-precipitation process of the carbonate precursors. It has been shown in previous reports [40] that particle morphologies, size distributions, and stoichiometry of carbonate precursors can be affected by the pH of the solution during the co-precipitation process. Based on the previous studies, the pH values are selected as 8.5, 8.2, 7.8 and 7.5, respectively, in the co-precipitation of the precursors in this study.

The XRD patterns of the carbonate precursors synthesized at different pH are shown in Fig. 1(a). It can be seen that the precursor co-precipitated at pH = 7.5 has a pure phase that can be indexed as $MnCO_3$ rhodochrosite (space group $R\bar{3}c$, PDF NO. 01-0981). When the pH is increased from 7.5 to 7.8, 8.2 and 8.5, respectively, an impurity appears which shows diffraction peaks at 11.5°, 23.1°, 34.6° and 39.1°. This impurity

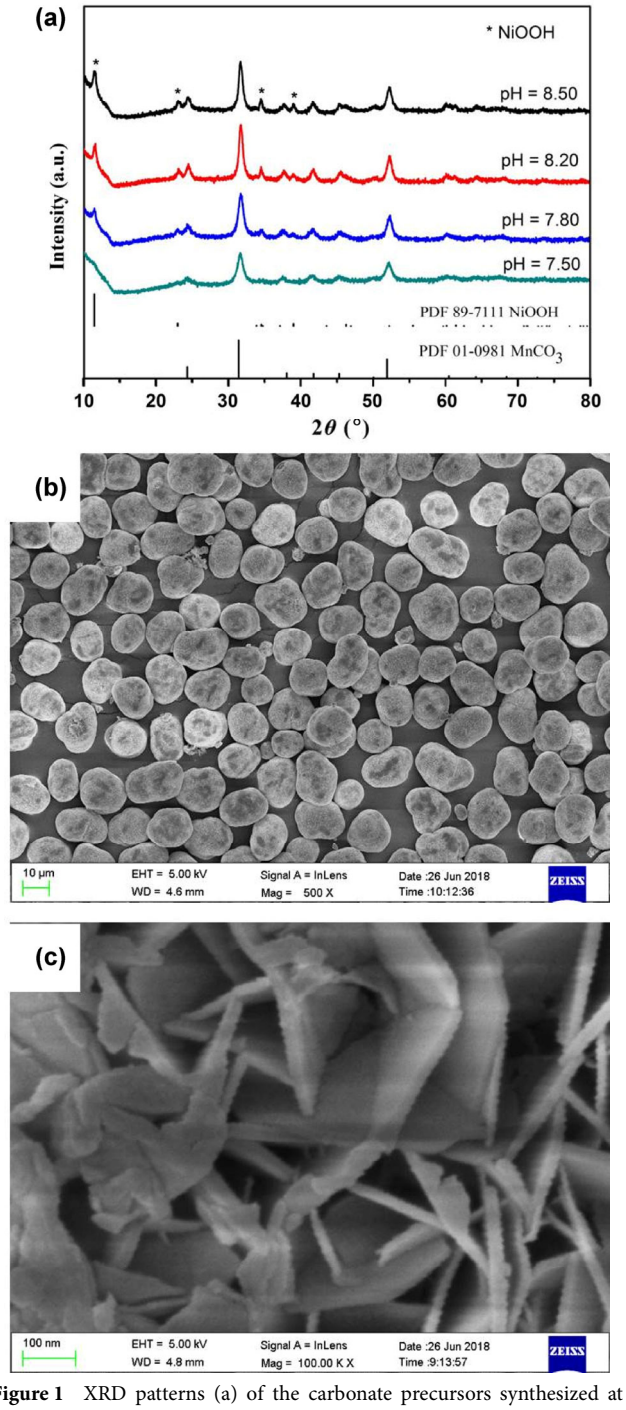

Figure 1 XRD patterns (a) of the carbonate precursors synthesized at different pH and the SEM images ((b) and (c)) of the carbonate precursor precipitated at pH = 7.5.

can be indexed as NiOOH (PDF No. 89-7111). The SEM images of the pure carbonate precursor co-precipitated at pH = 7.5 are shown in Figs. 1(b) and 1(c). The SEM images show that the carbonate precursors have typical hierarchical structures, with nanoplates as primary structures and microspheres as secondary structures. The thickness of the nanoplates (primary structures of the precursors) is about 10–20 nm. The diameters of the microspheres (secondary structures of the precursors) are about 10–15 μm. The SEM images of the carbonate precursors precipitated at the other pH values are shown in Fig. S2 in the ESM. As the figures shown, all the precipitates have hierarchical structures, with nanoplates (thickness: 8–30 nm) as the primary structures and microspheres (diameter: 5–20 μm) as the secondary structures.

Figure 2(a) shows the XRD patterns of the LLOs lithiated with the carbonate precursors that precipitated at different pH values. The layered oxides are labeled as LMNCO-8.5, LMNCO-8.2, LMNCO-7.8 and LMNCO-7.5, respectively, when their carbonate precursors are precipitated at the pH values of 8.5, 8.2, 7.8 and 7.5. It can be seen that all the samples have pure phase, which can be indexed as the layered α-$NaFeO_2$ structure (space group: $R\bar{3}m$). Several very small diffraction peaks at 20°–25° can be found in the enlarged XRD patterns, which should be indexed as the superlattice (020), (110) and ($\bar{1}11$) of Li_2MnO_3 (space group: $C2/m$). The well-split peaks of (006)/(012) at $2\theta = 38°$ and (018)/(110) at $2\theta = 65°$ of all the four materials suggest that the materials have well-defined layered structures with low

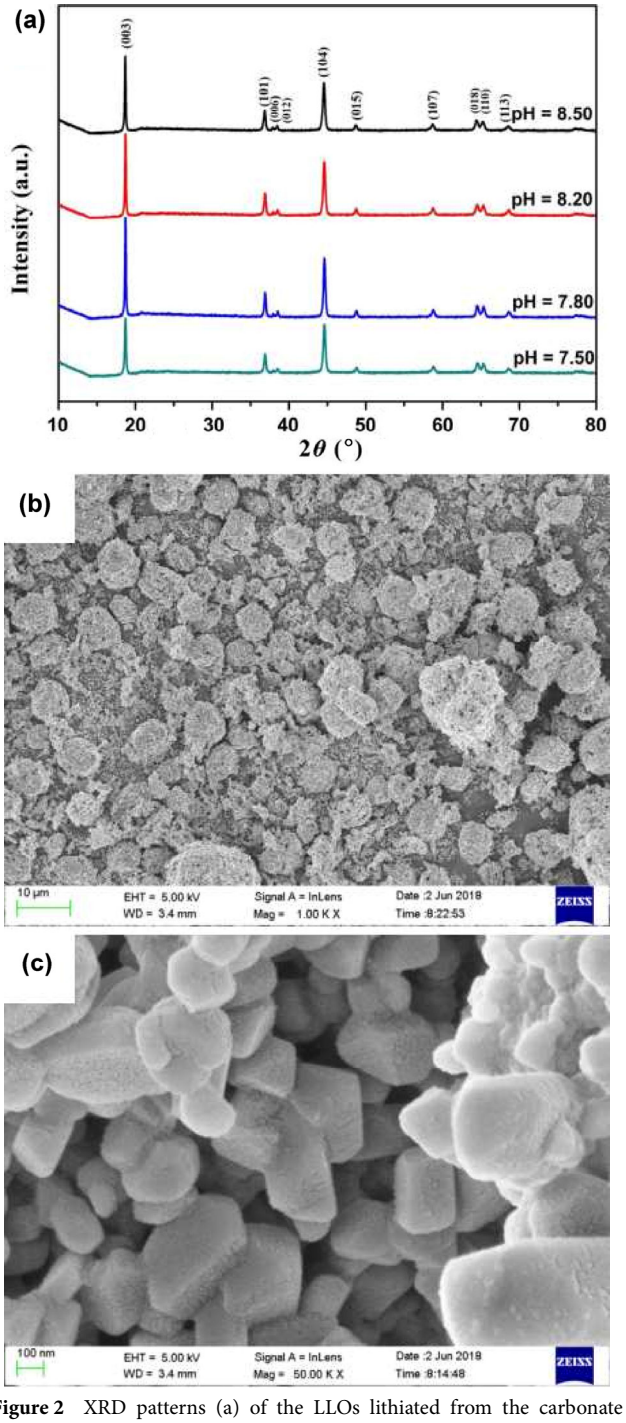

Figure 2 XRD patterns (a) of the LLOs lithiated from the carbonate precursors that precipitated at different pH values and the SEM images ((b) and (c)) of LLOs lithiated from the carbonate precursors that precipitated at pH = 7.5.

cations disordering [41]. Figures 2(b) and 2(c) show the SEM images of the lithium-rich layered oxide synthesized with the precursors precipitated at pH = 7.5. It can be seen that the lithium-rich layered oxides, like their carbonate precursors, have hierarchical structures. While the primary structures change from nanoplates to nanoparticles, the secondary structures remain as microspheres. The SEM images of the LLOs synthesized with the precursors that precipitated at other pH values are shown in Fig. S3 in the ESM.

Figure S4 in the ESM shows a STEM-HAADF analysis with EDX measurement of the oxide LMNCO-8.5. It shows that the Mn, Co, Ni and O elements are well mixed and homogeneously distributed within the whole particle, indicating that the particle should not be a physical mixture. Figure 3 shows the HRTEM image of the LMNCO-8.5 (Fig. 3(a)), the fast Fourier transform (FFT) to two different nanodomains in the nanoparticle (Figs. 3(b) and 3(c)), and the simulated SAED patterns for hexagonal $LiMO_2$-type phase and monoclinic Li_2MnO_3-type phase (Figs. 3(d) and 3(e)). Two nanodomains, shown as domain (I) and domain (II), with different lattice arrangements can be identified in the HRTEM image. The FFT to nanodomain (I) can be indexed to $[10\bar{1}\bar{1}]_H$ zone axis of hexagonal $R\bar{3}m$ $LiMO_2$ phase (Fig. 3(b)), whereas the FFT to nanodomain (II) can be indexed to $[001]_M$ zone axis of monoclinic $C2/m$ Li_2MO_3 phase (Fig. 3(c)). Figures 3(d) and 3(e) further demonstrate the simulated SAED patterns for the $R\bar{3}m$ phase and the monoclinic $C2/m$ phase, where the most visible dots in the experimental pattern are highlighted by white and blue circles. From the figures we can see that all white circles can coincide very well, which indicates the topotactic coexistence nature of two integrate phases. To further validate the opinion that the hexagonal $LiMO_2$ phase is embedded in the layered monoclinic Li_2MnO_3 phase in the LMNCO-8.5 particle, SAED experiments on the whole particle were carried, with the results shown in Fig. S5 in the ESM. No spots are split into satellites, and all the diffraction spots are quite uniform and well-spaced. Hence, Fig. S5(b) in the ESM is further illustrated in two orientation matrices with two different colors (red and blue).

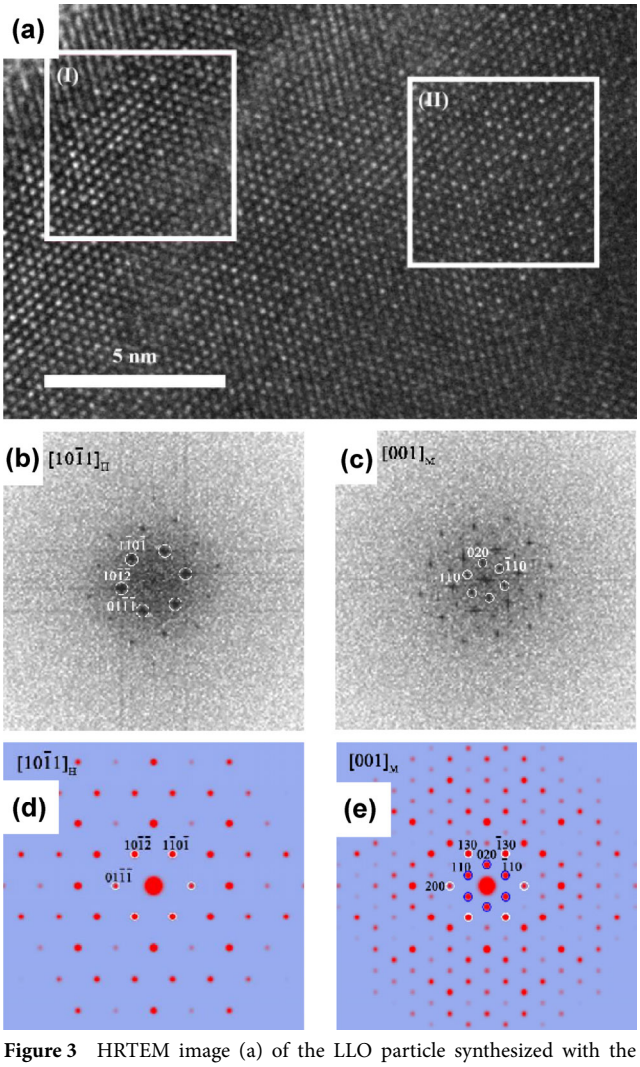

Figure 3 HRTEM image (a) of the LLO particle synthesized with the precursor precipitated at pH = 8.5, the FFT to two different nanodomains ((b) and (c)) in the nanoparticle, and the simulated SAED patterns ((d) and (e)) for hexagonal $LiMO_2$ phase and monoclinic Li_2MnO_3 phase.

Chemical analysis using ICP-AES is applied to determine the actual components of the materials. Table 1 shows the results of the ICP-AES analysis. In general, the measured compositions of the materials are in good agreement with the target composition ($Li_{1.17}Mn_{0.50}Ni_{0.24}Co_{0.09}O_2$). With careful analysis, it can be found that the ratios of Li/Ni in the measured chemical composition decrease when the pH values increase in the co-precipitation process. The Li/Ni ratios are 5.17, 4.92, 4.88, and 4.64, respectively, for LMNCO-7.5, LMNCO-7.8, LMNCO-8.2, and LMNCO-8.5. Therefore, the actual chemical stoichiometry of these lithium-rich layered oxides are influenced by the pH of the precursor co-precipitation reaction.

The voltage-capacity curves and dQ/dV profiles of the first charge-discharge cycle at the rate of 0.1 C (1 C = 200 mA·g^{-1}) in the voltage range of 2.0–4.8 V (versus Li$^+$/Li) for the LMNCO-8.5 are presented in Fig. 4. The initial charge curve in Fig. 4(a) is composed of a sloping region (below 4.4 V) and a long plateau region (above 4.4 V). While the sloping region is supposed to be due to the oxidation of $Ni^{2+} \rightarrow Ni^{4+}$ and $Co^{3+} \rightarrow Co^{4+}$ from the $LiMO_2$ phase, the long plateau is corresponding to the irreversible electrochemical activation of Li_2MnO_3 phase in the material. The discharge curve in Fig. 4(a) is composed of only a sloping region without any plateau part. In this first charge-discharge cycle for the LMNCO-8.5, the specific charge capacity is about 333 mAh·g^{-1}, and the reversible discharge specific capacity is about 263 mAh·g^{-1}, with initial Coulombic efficiency of 79.0% (and an irreversible capacity of only 70 mAh·g^{-1}). The dQ/dV profiles corresponding to the voltage-capacity curves in Fig. 4(a) are presented in Fig. 4(b). While there are three peaks, at the voltage of 3.82, 3.94, and 4.52 V, respectively, in the dQ/dV profiles of charge process, only two peaks, at the voltages of 3.73 and 3.41 V, respectively, are obvious in the dQ/dV profiles of discharge process. The peaks at 3.82 V in the charge process and 3.41 V in the discharge process are corresponding to the oxidation/reduction of Ni^{2+}/Ni^{4+} in the $LiMO_2$ phase; and the peaks at 3.94 V in the charge process and 3.73 V in the discharge process are due to the oxidation/reduction of Co^{3+}/Co^{4+} in the $LiMO_2$ phase in the material. The peak at 4.52 V in the charge process corresponds to the oxidation of O^{2-} in the Li_2MnO_3 phase in the material, accompanied by the Li$^+$ insertion into the electrolyte. Since there is no obvious dQ/dV peak in the discharge process corresponding to this O^{2-} oxidation peak,

Table 1 The chemical compositions, measured by ICP-AES, of the materials that have precursors co-precipitated at different pH. The target composition is $Li_{1.17}Mn_{0.50}Ni_{0.24}Co_{0.09}O_2$

Sample	Measured composition	Li/Ni
LMNCO-8.5	$Li_{1.16}Mn_{0.50}Ni_{0.25}Co_{0.09}O_2$	4.64
LMNCO-8.2	$Li_{1.17}Mn_{0.50}Ni_{0.24}Co_{0.09}O_2$	4.88
LMNCO-7.8	$Li_{1.18}Mn_{0.49}Ni_{0.24}Co_{0.09}O_2$	4.92
LMNCO-7.5	$Li_{1.19}Mn_{0.48}Ni_{0.23}Co_{0.09}O_2$	5.17

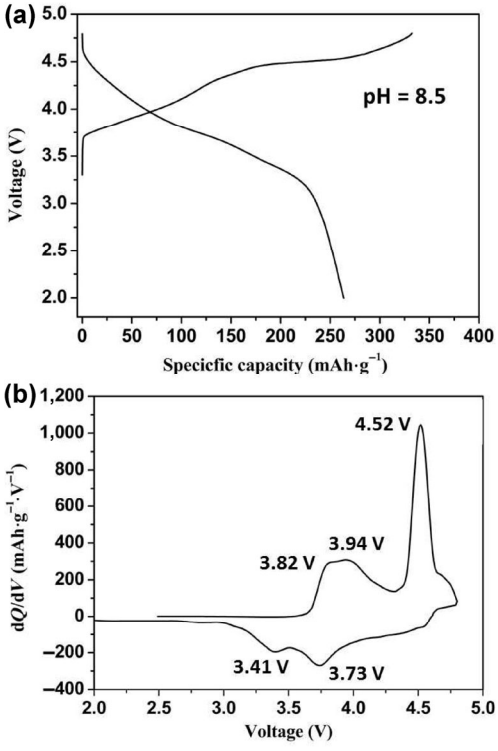

Figure 4 The voltage-capacity curves (a) and dQ/dV profiles (b) in the first charge-discharge cycle for LMNCO-8.5 at the rate of 0.1 C (1 C = 200 mA·g^{-1}) in the voltage range of 2.0–4.8 V (vs. Li$^+$/Li).

it implies that this oxidation of O^{2-} in the Li_2MnO_3 phase is irreversible. The voltage-capacity curves and dQ/dV profiles of the first charge-discharge cycle at the rate of 0.1 C in the voltage range of 2.0–4.8 V for the other three samples (LMNCO-8.2, LMNCO-7.8, and LMNCO-7.5) are presented in Fig. S6 in the ESM. As expected, the voltage-capacity curves and the dQ/dV profiles for all the samples have the same shapes.

Figures 5(a)–5(d) show the voltage–capacity curves in discharge processes in the 2nd, 10th, 20th and 50th cycles for all the materials. As the figures show, in all the cycles, while the LMNCO-8.5 has the highest discharge voltage, the LMNCO-7.5 has the lowest discharge voltage, and the LMNCO-8.2 and the LMNCO-7.8 have discharge voltages in between. Figure 5(e) shows the average discharge voltages in discharge process of the materials from the 3rd to the 50th cycles. From the figure, it can be seen that the higher pH values in which the precursors prepared, the higher average discharge voltage it has in the discharge process. Specifically, the LMNCO-8.5 shows the highest average discharge voltages in all the charge-discharge cycles. The average discharge voltages are 3.65 V in the 3rd cycle and 3.56 V in the 50th cycle. On the contrary, the LMNCO-7.5 shows the lowest average discharge voltages in all the charge-discharge cycles. The average discharge voltages are 3.56 V in the 3rd cycle and 3.44 V in the 50th cycle. This average discharge voltage for the LMNCO-8.5 in this work (3.65 V) is better than the average discharge voltage for the high nickel content component $0.5Li_2MnO_3{\cdot}0.5LiNi_{0.8}Co_{0.1}Mn_{0.1}O_2$ in the literature (3.62 V) [42]. Difference between the average charge voltage and average discharge voltage (ΔV) is another parameter to show the polarization of cathode materials during cycling. While the LMNCO-8.5 shows the smallest ΔV in all the charge-discharge cycles, the LMNCO-7.5 has the highest ΔV in all the cycles. For example, the ΔVs for the LMNCO-8.5 are 0.26 V in the 3rd cycle and 0.28 V in the 50th cycle; and the ΔVs for the LMNCO-7.5 are 0.32 V in the 3rd cycle and 0.36 V in the 50th cycle.

The dQ/dV profiles of discharge processes in the 2nd, 10th, 20th and 50th cycles of the materials are shown in Fig. 6. While the reduction peaks around 3.7 V correspond to the reduction of Ni^{4+}/Ni^{2+} and Co^{4+}/Co^{3+}, the reduction peaks around 3.2 V indicates the reduction of Mn^{4+}/Mn^{3+} in these layered-structured materials. Figure 6 indicates that, when the pH values in the synthesis increased from 7.5 to 8.5, the dQ/dV reduction peaks around 3.7 V shift to higher voltages and become stronger and sharper. For example, in the 2nd charge-discharge cycle (Fig. 6(a)), the dQ/dV reduction peaks are at the voltages of 3.69, 3.71, 3.73, and 3.75 V, respectively, and the intensities of the peaks

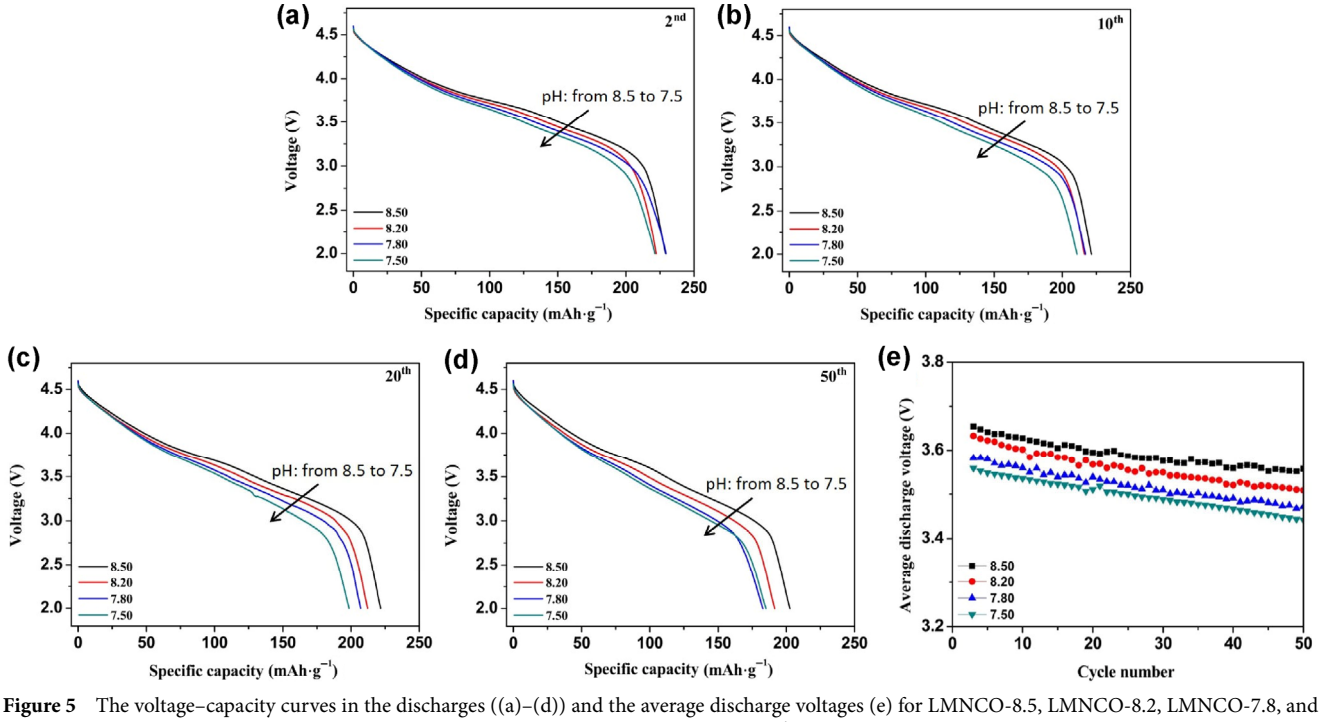

Figure 5 The voltage–capacity curves in the discharges ((a)–(d)) and the average discharge voltages (e) for LMNCO-8.5, LMNCO-8.2, LMNCO-7.8, and LMNCO-7.5. All the materials were charge-discharged at the rate of 0.1 C (1 C = 200 mA·g^{-1}) in the voltage ranges of 2.0–4.6 V (versus Li$^+$/Li).

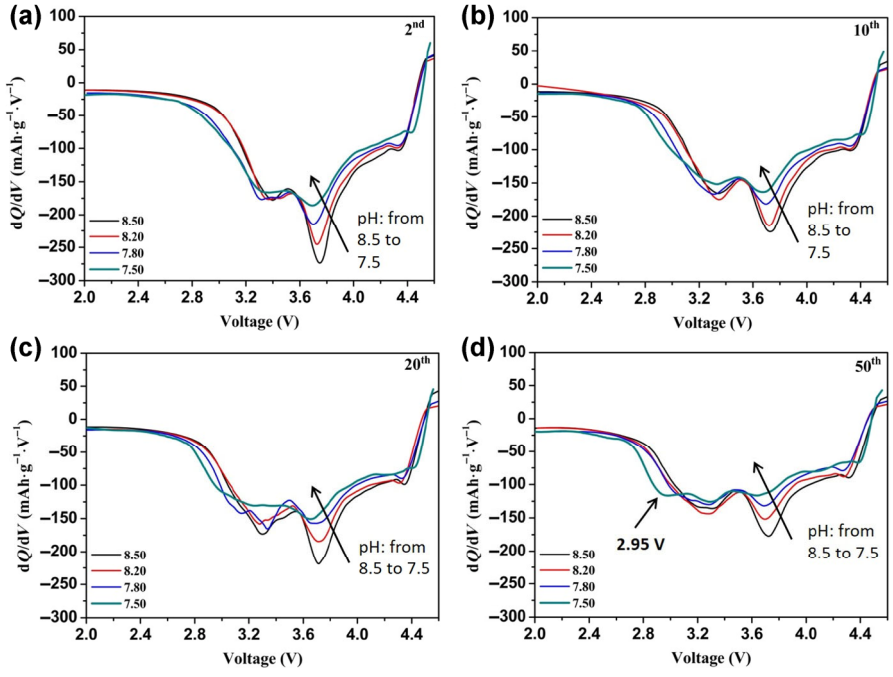

Figure 6 The dQ/dV profiles in discharge processes in the 2nd, 10th, 20th, and 50th cycle for LMNCO-8.5, LMNCO-8.2, LMNCO-7.8, and LMNCO-7.5. All the materials were charge-discharged at the rate of 0.1 C (1 C = 200 mA·g^{-1}) in the voltage ranges of 2.0–4.6 V (versus Li$^+$/Li).

are 187, 215, 247 and 277 mAh·g^{-1}·V^{-1}, respectively, for the materials that synthesized at the pH values of 7.5, 7.8, 8.2 and 8.5. In the 50th cycle (Fig. 6(d)), the dQ/dV reduction peaks are at 3.64 and 3.71 V, respectively, and the intensities of the peaks are 118 and 180 mAh·g^{-1}·V^{-1}, respectively, for LMNCO-7.5 and LMNCO-8.5. This phenomenon means that the LMNCO-8.5, among all the samples, have the highest specific capacity from the reduction of Ni^{4+}/Ni^{2+} and Co^{4+}/Co^{3+}. The dQ/dV reduction peaks around 3.2 V have the same, although much weaker, trend. After prolong cycling, the LMNCO-7.5 shows a clear dQ/dV reduction peak at around 2.9 V in the 50th charge-discharge cycle, while no peaks at ~ 2.9 V can be found in the dQ/dV profiles for the LMNCO-8.5 sample (Fig. 6(d)). Since the reduction peak at 2.9 V is indicative of Mn^{4+}/Mn^{3+} in spinel-like phase, this clear reduction peak proves the formation of spinel structure in the layered-structured materials during cycling. On the contrary to the LMNCO-7.5, the LMNCO-8.5 has the smallest layered-to-spinel structure evolution. Spinel structure formation in layered-structures is described as the results of migration and dissolution of transition metal ions in the materials.

Figure 7(a) shows the discharge capacities versus cycle numbers for all the four samples at the rate of 0.1 C in the voltage window of 2.0–4.6 V (after initial cycling in the range of 2.0–4.8 V). The LMNCO-8.5 exhibits the highest discharge capacities from the 3rd cycle to the 50th cycle. On the contrary, LMNCO-7.5 and LMNCO-7.8 show the lowest discharge capacities from the 3rd cycle. After 50 charge-discharge cycles, the discharge capacities are 198, 191, 183 and 185 mAh·g^{-1} for LMNCO-8.5, LMNCO-8.2, LMNCO-7.8 and LMNCO-7.5, respectively. Figure 7(b) shows the typical voltage-capacity curves of the LMNCO-8.5 at the rates of 0.1, 0.2, 0.5, 1, 2, and 5 C, respectively. And when the LMNCO-8.5 was charge-discharged at varied rates from 0.1 to 5 C with five cycles in each rate and finally returned back to 0.1 C rate, it showed a capacity of 210 mAh·g^{-1}, with capacity retention of 94.5%, indicating that the LMNCO-8.5 had very stable structures at different rates. Figure 7(c) shows the discharge capacity versus the cycle number plots of the LMNCO-8.5 at the rates of 1 C in the range of 2.0–4.6 V (after initial cycling in the range of 2.0–4.8 V). The discharge specific capacity of the sample is 177 mAh·g^{-1} in the 2nd cycle, which decreases to 166 mAh·g^{-1} after 100 charge–discharge cycles, with 94% capacity retention. In contrast, for the LMNCO-7.8 and the LMNCO-7.5, the capacity retentions are only 72% and 73%, respectively, after 100 cycles. Thus, the LMNCO-8.5 exhibits a much more stable rate capability, together with higher discharge voltages, than the LMNCO-7.5.

To further understand the reasons of different electrochemical performance among the four samples prepared at different pH, the electrochemical impedance spectroscopy (EIS) has been measured after the 1st and the 50th cycle to identify the evolution of charge transfer resistance and electrode–electrolyte interphase resistance. The plots are showed in Figs. 8(a)–8(d). All the EIS plots consist of one semicircle in the high-frequency region and a slope in the low-frequency region. The semicircle in the high frequency region is produced by overlapping of two different semicircles, in which the semicircle at high frequency is related to the surface-electrolyte interface resistance (R_{sf}), and the semicircle at the high-to-medium frequency is assigned to the charge transfer resistance (R_{ct}). The slope in the low frequency region corresponds to a semi-infinite Warburg diffusion process in the bulk. In addition, the intercept of the highest frequency semicircle with the x-axis represents the ohmic resistance R_s. The equivalent circuit presented in Fig. 8(e) is used for fitting EIS data, and the corresponding fitting results are listed in Table 2. All samples show small ohmic resistance R_s, with the LMNCO-8.5 having the lowest R_s (2.8 Ω) after the 1st charge-discharge cycle. In contrast to the increasing of R_s, R_{sf} + R_{ct} undergoes a large decrease among all the samples, indicating the decreased ionic resistance and suppressing of phase transition during cycling. Particularly, the LMNCO-8.5 showed the smallest R_{sf} + R_{ct} value of 4.2 Ω after 50 cycles. The decrease in R_{sf} + R_{ct} during cycling explains the superior rate performance and high average discharge voltage.

Guo and Wan group synthesized $0.5Li_2MnO_3{\cdot}0.5LiNi_{0.8}Co_{0.1}Mn_{0.1}O_2$ (LL-811) and $0.5Li_2MnO_3{\cdot}0.5LiNi_{1/3}Co_{1/3}Mn_{1/3}O_2$ (LL-333) that have different Ni content in the materials, and showed that

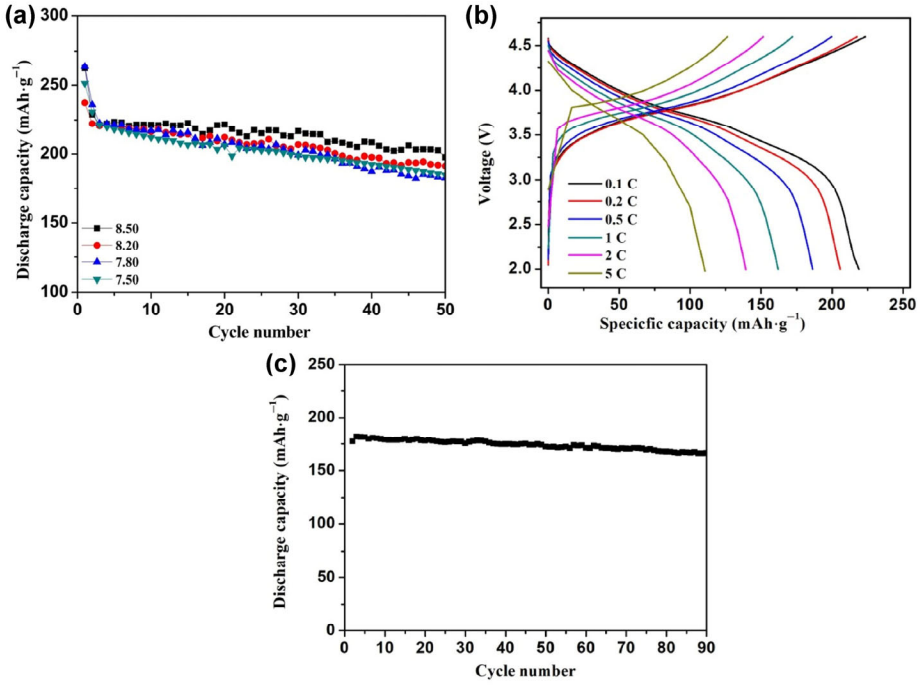

Figure 7 The discharge capacities versus cycle numbers for the materials (a), the typical voltage-capacity curves at different rates (b), and the cyclibility plot at the rate of 1 C (c) of the LMNCO-8.5. The discharge capacities versus cycle numbers for the materials were tested at the rate of 0.1 C in the voltage window of 2.0–4.6 V. The typical voltage-capacity curves of the LMNCO-8.5 were tested at the rates of 0.1, 0.2, 0.5, 1, 2, and 5 C, respectively; the cyclibility plot of the LMNCO-8.5 was tested at the rate of 1 C in the range of 2.0–4.6 V.

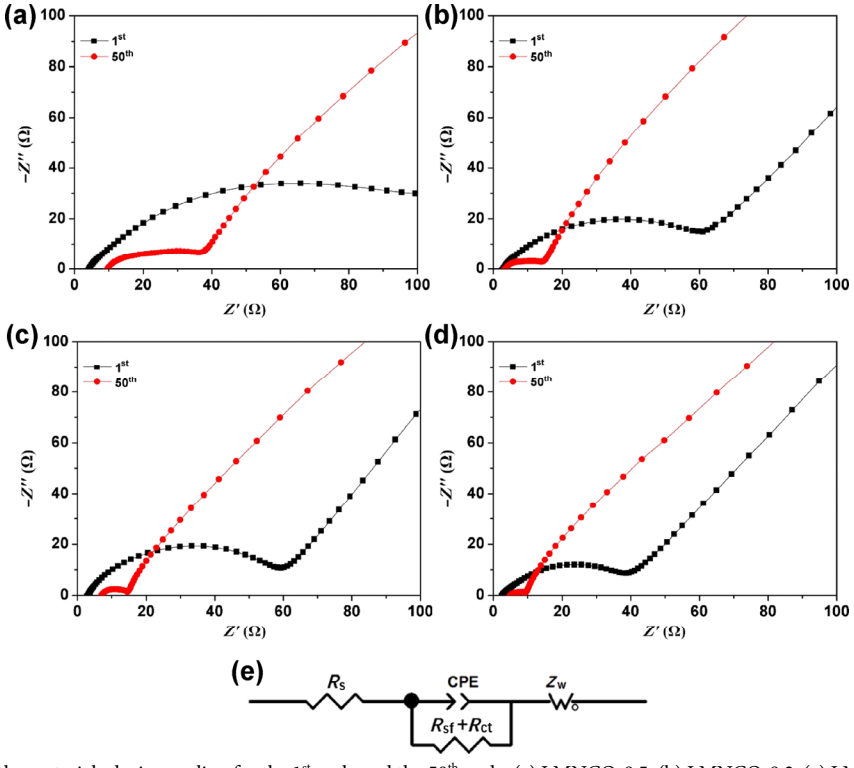

Figure 8 Nyquist plots of the materials during cycling for the 1st cycle and the 50th cycle. (a) LMNCO-8.5, (b) LMNCO-8.2, (c) LMNCO-7.8, (d) LMNCO-7.5 (inset images are corresponding Nyquist plots with magnification); (e) the corresponding equivalent circuit model.

higher Ni content material LL-811 exhibited higher average discharge voltage than lower Ni content material LL-333 [42]. They suggested that the higher Ni content can not only serve as structure stabilizing pillar, but also result in the migration of nickel ions to Li vacancies in TM layers, and nickel ions can reversibly migrate between TM layer and the interlayer during charging-discharging process. Moreover, the nickel ions can improve the d-p hybridization to restrain the Jahn-Teller effect of Mn^{3+}. From the electrochemical properties of the Li-rich layered oxide materials that have been synthesized at different pH, it notably reveals that, lower Li/Ni ratio (higher Ni content) in materials could improve the structural stability and suppress voltage decay by pillar effect. Also, materials with lower ratio of Li/Ni value have better cycling stability, which roots from the decrease of surface-electrolyte interface resistance and charge transfer resistance.

4 Conclusions

Lithium-rich layered oxide materials with novel composition of $Li_{1.17}Mn_{0.50}Ni_{0.24}Co_{0.09}O_2$ have been prepared by carbonate co-precipitation method and their electrochemical properties have been measured as the cathode materials for Li-ion batteries. It has been shown that the exact chemical compositions, thus the Li/Ni ratios, of the samples are influenced by the pH values in the synthesis processes. The $Li_{1.17}Mn_{0.50}Ni_{0.24}Co_{0.09}O_2$ that synthesized at pH = 8.5 has the lowest Li/Ni value of 4.64, and it delivers a reversible discharge capacity of 263 $mAh{\cdot}g^{-1}$ with 79.0% initial Coulombic efficiency in the first charge-discharge cycle and 94% capacity retention after 100 cycles at 1 C. Especially, this material exhibits an average discharge voltage of 3.65 V in the cycle and a voltage decay of only 0.09 V after 50 cycles. All these prove that low ratio of Li/Ni value with high Ni content can improve the structure stability and mitigate the voltage decay during charge-discharge cycling for the Li-rich layered oxides. Hopefully, our work can help to develop a direction to mitigate voltage fade through the combination of tuning composition and optimizing synthesis method.

Acknowledgements

We thank the National Natural Science Foundation of China (No. 21271145), the National Science Foundation of Hubei Province (No. 2015CFB537) and the Science and Technology Innovation Committee of Shenzhen Municipality (No. JCYJ20170306171321438) for the financial support for this investigation.

Electronic Supplementary Material: Supplementary material (SEM images of the carbonate precursors and the lithium-rich layered oxides synthesized with the precursors; TEM images, SAED experiments and STEM-HAADF analysis with EDX measurement of the Li-rich layered oxide LMNCO-8.5; voltage–capacity curves and dQ/dV profiles in the first charge-discharge cycle at the rate of 0.1 C for materials LMNCO-8.2, LMNCO-7.8, and LMNCO-7.5) is available in the online version of this article at https://doi.org/ 10.1007/s12274-019-2588-0.

References

[1] Li, M.; Lu, J.; Chen, Z. W.; Amine, K. 30 years of lithium-ion batteries. *Adv. Mater.* **2018**, *30*, 1800561.

[2] Zeng, X. Q.; Li, M.; Abd El-Hady, D.; Alshitari, W.; Al-Bogami, A. S.; Lu, J.; Amine, K. Commercialization of lithium battery technologies for electric vehicles. *Adv. Energy Mater.* **2019**, *9*, 1900161.

[3] Liu, Y. Y.; Zhu, Y. Y.; Cui, Y. Challenges and opportunities towards fast-charging battery materials. *Nat. Energy* **2019**, *4*, 540–550.

[4] Yu, H. J.; Zhou, H. S. High-energy cathode materials (Li_2MnO_3-$LiMO_2$) for lithium-ion batteries. *J. Phys. Chem. Lett.* **2013**, *4*, 1268–1280.

[5] Ye, D. L.; Wang, L. Z. Li_2MnO_3 based Li-rich cathode materials: Towards a better tomorrow of high energy lithium ion batteries. *Mater. Technol.* **2014**, *29*, A59–A69.

[6] Jarvis, K. A.; Deng, Z. Q.; Allard, L. F.; Manthiram, A.; Ferreira, P. J. Atomic structure of a lithium-rich layered oxide material for lithium-ion batteries: Evidence of a solid solution. *Chem. Mater.* **2011**, *23*, 3614–3621.

[7] Johnson, C. S.; Kim, J. S.; Lefief, C.; Li, N.; Vaughey, J. T.; Thackeray, M. M. The significance of the Li_2MnO_3 component in "composite" $xLi_2MnO_3{\cdot}(1–x)$ $LiMn_{0.5}Ni_{0.5}O_2$ electrodes. *Electrochem. Commun.* **2004**, *6*, 1085–1091.

[8] Thackeray, M. M.; Kang, S. H.; Johnson, C. S.; Vaughey, J. T.; Hackney, S. A. Comments on the structural complexity of lithium-rich $Li_{1+x}M_{1-x}O_2$ electrodes (M = Mn, Ni, Co) for lithium batteries. *Electrochem. Commun.* **2006**, *8*, 1531–1538.

[9] Sathiya, M.; Rousse, G.; Ramesha, K.; Laisa, C. P.; Vezin, H.; Sougrati, M. T.; Doublet, M. L.; Foix, D.; Gonbeau, D.; Walker, W. et al. Reversible anionic redox chemistry in high-capacity layered-oxide electrodes. *Nat. Mater.* **2013**, *12*, 827–835.

[10] Sathiya, M.; Abakumov, A. M.; Foix, D.; Rousse, G.; Ramesha, K.; Saubanère, M.; Doublet, M. L.; Vezin, H.; Laisa, C. P. et al. Origin of voltage decay in high-capacity layered oxide electrodes. *Nat. Mater.* **2015**, *14*, 230–238.

[11] McCalla, E.; Abakumov, A. M.; Saubanère, M.; Foix, D.; Berg, E. J.; Rousse, G.; Doublet, M. L.; Gonbeau, D.; Novák, P. et al. Visualization of O-O peroxo-like dimers in high-capacity layered oxides for Li-ion batteries. *Science* **2015**, *350*, 1516–1521.

[12] Seo, D. H.; Lee, J.; Urban, A.; Malik, R.; Kang, S. Y.; Ceder, G. The structural and chemical origin of the oxygen redox activity in layered and cation-disordered Li-excess cathode materials. *Nat. Chem.* **2016**, *8*, 692–697.

[13] Saubanère, M.; McCalla, E.; Tarascon, J. M.; Doublet, M. L. The intriguing question of anionic redox in high-energy density cathodes for Li-ion batteries. *Energy Environ. Sci.* **2016**, *9*, 984–991.

[14] Luo, K.; Roberts, M. R.; Hao, R.; Guerrini, N.; Pickup, D. M.; Liu, Y. S.; Edström, K.; Guo, J. H.; Chadwick, A. V.; Duda, L. C. et al. Charge-compensation in 3d-transition-metal-oxide intercalation cathodes through the generation of localized electron holes on oxygen. *Nat. Chem.* **2016**, *8*, 684–691.

[15] Gu, M.; Belharouak, I.; Zheng, J. M.; Wu, H. M.; Xiao, J.; Genc, A.; Amine, K.; Thevuthasan, S.; Baer, D. R.; Zhang, J. G. et al. Formation of the spinel phase in the layered composite cathode used in Li-ion batteries. *ACS Nano* **2013**, *7*, 760–767.

[16] Croy, J. R.; Kim, D.; Balasubramanian, M.; Gallagher, K.; Kang, S. H.; Thackeray, M. M. Countering the voltage decay in high capacity $xLi_2MnO_3{\cdot}(1–x)LiMO_2$ electrodes (M = Mn, Ni, Co) for Li^+-ion batteries. *J. Electrochem. Soc.* **2012**, *159*, A781–A790.

[17] Mohanty, D.; Sefat, A. S.; Kalnaus, S.; Li, J. L.; Meisner, R. A.; Payzant, E. A.; Abraham, D. P.; Wood, D. L.; Daniel, C. Investigating phase transformation in the $Li_{1.2}Co_{0.1}Mn_{0.55}Ni_{0.15}O_2$ lithium-ion battery cathode during high-voltage hold (4.5 V) via magnetic, X-ray diffraction and electron microscopy studies. *J. Mater. Chem. A* **2013**, *1*, 6249–6261.

[18] Croy, J. R.; Gallagher, K. G.; Balasubramanian, M.; Chen, Z. H.; Ren, Y.; Kim, D. H.; Kang, S. H.; Dees, D. W.; Thackeray, M. M. Examining hysteresis in composite $xLi_2MnO_3{\cdot}(1–x)LiMO_2$ cathode structures. *J. Phys. Chem. C* **2013**, *117*, 6525–6536.

[19] Ito, A.; Shoda, K.; Sato, Y.; Hatano, M.; Horie, H.; Ohsawa, Y. Direct observation of the partial formation of a framework structure for Li-rich layered cathode material $Li[Ni_{0.17}Li_{0.2}Co_{0.07}Mn_{0.56}]O_2$ upon the first charge and discharge. *J. Power Sources* **2011**, *196*, 4785–4790.

[20] Mohanty, D.; Li, J. L.; Abraham, D. P.; Huq, A.; Payzant, E. A.; Wood III, D. L.; Daniel, C. Unraveling the voltage-fade mechanism in high-energy-density lithium-ion batteries: Origin of the tetrahedral cations for spinel conversion. *Chem. Mater.* **2014**, *26*, 6272–6280.

[21] Gallagher, K. G.; Croy, J. R.; Balasubramanian, M.; Bettge, M.; Abraham, D. P.; Burrell, A. K.; Thackeray, M. M. Correlating hysteresis and voltage fade in lithium- and manganese-rich layered transition-metal oxide electrodes. *Electrochem. Commun.* **2013**, *33*, 96–98.

[22] Mohanty, D.; Kalnaus, S.; Meisner, R. A.; Rhodes, K. J.; Li, J. L.; Payzant, E. A.; Wood III, D. L.; Daniel, C. Structural transformation of a lithium-rich $Li_{1.2}Co_{0.1}Mn_{0.55}Ni_{0.15}O_2$ cathode during high voltage cycling resolved by *in situ* X-ray diffraction. *J. Power Sources* **2013**, *229*, 239–248.

[23] Xu, B.; Fell, C. R.; Chi, M. F.; Meng, Y. S. Identifying surface structural changes in layered Li-excess nickel manganeseoxides in high voltage lithium ion batteries: A joint experimental and theoretical study. *Energy Environ. Sci.* **2011**, *4*, 2223–2233.

[24] Zheng, J. M.; Gu, M.; Xiao, J.; Zuo, P. J.; Wang, C. M.; Zhang, J. G. Corrosion/fragmentation of layered composite cathode and related capacity/voltage fading during cycling process. *Nano Lett.* **2013**, *13*, 3824–3830.

[25] Liu, W.; Oh, P.; Liu, X. E.; Myeong, S.; Cho, W.; Cho, J. Countering voltage decay and capacity fading of Lithium-rich cathode material at 60 °C by hybrid surface protection layers. *Adv. Energy Mater.* **2015**, *5*, 1500274.

[26] Yan, W. W.; Liu, Y. N.; Guo, S. W.; Jiang, T. Effect of defects on decay of voltage and capacity for $Li[Li_{0.15}Ni_{0.2}Mn_{0.6}]O_2$ cathode material. *ACS Appl. Mater. Interfaces* **2016**, *8*, 12118–12126.

[27] Singer, A.; Zhang, M.; Hy, S.; Cela, D.; Fang, C.; Wynn, T. A.; Qiu, B.; Xia, Y.; Liu, Z.; Ulvestad, A. et al. Nucleation of dislocations and their dynamics in layered oxide cathode materials during battery charging. *Nat. Energy* **2018**, *3*, 641–647.

[28] Ates, M. N.; Jia, Q. Y.; Shah, A.; Busnaina, A.; Mukerjee, S.; Abraham, K. M. Mitigation of layered to spinel conversion of a Li-rich layered metal oxide cathode material for Li-ion batteries. *J. Electrochem. Soc.* **2015**, *161*, A290-A301.

[29] Li, Q.; Li, G. S.; Fu, C. C.; Luo, D.; Fan, J. M.; Li, L. P. K^+-doped $Li_{1.2}Mn_{0.54}Co_{0.13}Ni_{0.13}O_2$: A novel cathode material with an enhanced cycling stability for lithium-ion batteries. *ACS Appl. Mater. Interfaces* **2014**, *6*, 10330–10341.

[30] Nayak, P. K.; Grinblat, J.; Levi, M.; Levi, E.; Kim, S.; Choi, J. W.; Aurbach, D. Al doping for mitigating the capacity fading and voltage decay of layered Li and Mn-rich cathodes for Li-ion batteries. *Adv. Energy Mater.* **2016**, *6*, 1502398.

[31] Nayak, P. K.; Grinblat, J.; Levi, E.; Levi, M.; Markovsky, B.; Aurbach, D. Understanding the influence of Mg doping for the stabilization of capacity and higher discharge voltage of Li- and Mn-rich cathodes for Li-ion batteries. *Phys. Chem. Chem. Phys.* **2017**, *19*, 6142–6152.

[32] Nayak, P. K.; Grinblat, J.; Levi, M.; Haik, O.; Levi, E.; Aurbach, D. Effect of Fe in suppressing the discharge voltage decay of high capacity Li-rich cathodes for Li-ion batteries. *J. Solid State Electrochem.* **2015**, *19*, 2781–2792.

[33] Zheng, J. M.; Gu, M.; Xiao, J.; Polzin, B. J.; Yan, P. F.; Chen, X. L.; Wang, C. M.; Zhang, J. G. Functioning mechanism of AlF_3 coating on the Li- and Mn-rich cathode materials. *Chem. Mater.* **2014**, *26*, 6320–6327.

[34] Sun, Y. K.; Lee, M. J.; Yoon, C. S.; Hassoun, J.; Amine, K.; Scrosati, B. The role of AlF_3 coatings in improving electrochemical cycling of Li-enriched nickel-manganese oxide electrodes for Li-ion batteries. *Adv. Mater.* **2012**, *24*, 1192–1196.

[35] Wu, Y.; Manthiram, A. High capacity, surface-modified layered $Li[Li_{(1-x)/3}Mn_{(2-x)/3}Ni_{x/3}Co_{x/3}]O_2$ cathodes with low irreversible capacity loss. *Electrochem. Solid-State Lett.* **2006**, *9*, A221–A224.

[36] Qiu, B.; Wang, J.; Xia, Y. G.; Wei, Z.; Han, S. J.; Liu, Z. P. Enhanced electrochemical performance with surface coating by reactive magnetron sputtering on lithium-rich layered oxide electrodes. *ACS Appl. Mater. Interfaces* **2014**, *6*, 9185–9193.

[37] Wang, Q. Y.; Liu, J.; Murugan, A. V.; Manthiram, A. High capacity double-layer surface modified $Li[Li_{0.2}Mn_{0.54}Ni_{0.13}Co_{0.13}]O_2$ cathode with improved rate capability. *J. Mater. Chem.* **2009**, *19*, 4965–4972.

[38] Zheng, F. H.; Yang, C. H.; Xiong, X. H.; Xiong, J. W.; Hu, R. Z.; Chen, Y.; Liu, M. L. Nanoscale surface modification of lithium-rich layered-oxide composite cathodes for suppressing voltage fade. *Angew. Chem., Int. Ed.* **2015**, *54*, 13058–13062.

[39] Zheng, J. M; Gu, M.; Genc, A.; Xiao, J.; Xu, P. H.; Chen, X. L.; Zhu, Z. H.; Zhao, W. B.; Pullan, L.; Wang, C. M. et al. Mitigating voltage fade in cathode materials by improving the atomic level uniformity of elemental distribution. *Nano Lett.* **2014**, *14*, 2628–2635.

[40] Ren, D.; Shen, Y.; Yang, Y.; Shen, L. X.; Levin, B. D. A.; Yu, Y. C.; Muller, D. A.; Abruna, H. D. Systematic optimization of battery materials: Key parameter optimization for the scalable synthesis of uniform, high-energy, and high stability $LiNi_{0.6}Mn_{0.2}Co_{0.2}O_2$ cathode material for lithium-ion batteries. *ACS Appl. Mater. Interfaces* **2017**, *9*, 35811–35819.

[41] Lee, D. K.; Park, S. H.; Amine, K.; Bang, H. J.; Parakash, J.; Sun, Y. K. High capacity $Li[Li_{0.2}Ni_{0.2}Mn_{0.6}]O_2$ cathode materials via a carbonate co-precipitation method. *J. Power Sources* **2006**, *162*, 1346–1350.

[42] Shi, J. L.; Zhang, J. N.; He, M.; Zhang, X. D.; Yin, Y. X.; Li, H.; Guo, Y. G.; Gu, L.; Wan, L. J. Mitigating voltage decay of Li-rich cathode material via increasing Ni content for lithium-ion batteries. *ACS Appl. Mater. Interfaces* **2016**, *8*, 20138–20146.